Dimension reduction method for ODE fluid models

Alexandre M. Tartakovsky [a] Alexander Panchenko [b] Kim Ferris [a]

[a] *Pacific Northwest National Laboratory, Richland, WA 99352*

[b] *Department of Mathematics, Washington State University, Pullman, WA 99164*

Abstract

We develop a new dimension reduction method for large size ODE systems obtained from a discretization of partial differential equations of viscous single and multiphase fluid flow. The method is also applicable to other large size classical particle systems with negligibly small variations of particle concentration. We propose a new computational closure for mesoscale balance equations based on numerical iterative deconvolution. To illustrate the computational advantages of the proposed reduction method, we use it to solve a system of Smoothed Particle Hydrodynamic ODEs describing single phase and two-phase layered Poiseuille flows driven by uniform and periodic (in space) body forces. For the single phase Poiseuille flow driven by the uniform force, the coarse solution was obtained with the zero-order deconvolution. For the single phase flow driven by the periodic body force and for the two-phase flows , the higher-order (the first- and second-order) deconvolutions were necessary to obtain a sufficiently accurate solution.

Key words: model reduction, ODEs, multiscale modeling, coarse integration, upscaling, closure problem, deconvolution

1 Introduction

Many diverse mathematical models of natural and technological systems have a common feature: their discrete approximations are systems of ordinary differential equations (ODEs), which can contain an enormous number of unknowns. Direct simulation of these models can be extremely expensive. This necessitates development of advanced algorithms for model (or dimension) reduction.

One classical approach to model reduction is volume averaging. Volume averaging can be applied to systems of ODEs describing Newtonian particle dynamics (e.g., [1]) and to partial differential equations (PDEs) (e.g., [2]). In the former case, the volume averaging reduces a system of ODEs to the system of PDEs describing the dynamics of the system averages. In the latter case, the system of PDEs describing a continuous process on one scale can be replaced by the system of PDEs describing the process on a larger scale (e.g., averaging of Navier-Stokes equations describing a pore-scale flow in a porous medium to obtain Darcy equations describing flow in the porous medium treated as a continuum). The resulting PDEs for averages usually contain non-local terms in the form of volume integrals of functions of the microscale variables, and the non-local PDEs do not present any computational advantage since a direct solution of such equations also requires solving the microscale equations. If an efficient and accurate closure could be found, the computational advantages of the volume averaging methods are achieved due to the fact that the averages vary slower in space and time than the original variables and PDEs for averages can be solved on a coarser grid and with a larger time step than the corresponding finer-scale ODEs or PDEs.

Development of the effective (closed) equations is the ultimate goal of any dimension reduction method as those equations provide the most computationally efficient method for a multiscale problem under consideration. Under certain length scale constraints (the constraints relating characteristic length scales of the derivatives of fine-scale variables, the characteristic length scales associated with averages, and the length scale of the domain), a closure can be obtained analytically [2]. Unfortunately, these constraints are usually satisfied for a relatively simple linear problems only. Examples of such problems include linear deformations of heterogeneous solids or single phase flow in porous media. For linear problems, PDE homogenization theory [3] also can be used to derive closed-form averaged PDEs. For non-linear problems, the application of homogenization methods becomes more difficult [4], [5]. Consequently, there are no homogenization results for many problems of practical interest, including multiphase flows with moving boundaries, nonlinear elastic wave propagation, and granular flows. Standard *ad hoc* closures for the PDEs obtained via volume averaging or homogenization were shown to fail for a number of nonlinear problems including crack- propagation and multicomponent reactive transport in porous

media [6–9].

For the multiscale systems with time scale separation (e. g., a small number of very heavy particles moving in a bath of very light particles), methods based on ODE perturbation theory and time homogenization can be employed. The patched dynamics and the equation-free method [10–13] could be used to estimate dynamics of averages if the closed-form PDEs for averages are not available. In the equation free-method, the averages are calculated from short bursts of fine-scale simulations in small parts of a computational domain. Other mathematical methods for dimension reduction include the optimal prediction methods [14,15] based on the projection operator formalism [16,17], renormalization group analysis [18], stochastic mode elimination [19], and cluster expansions [20–23]. Additional references on ODE dimension reduction and time homogenization can be found in a recent book [24].

In general, these methods produce reasonable results for ODE systems of the statistical mechanical type, characterized by fast mixing, short relaxation times, and approximate ergodicity. A statistical mechanical system quickly forgets the initial conditions and, during the observation time, tends to reach most points on the constant energy surface in phase space. In contrast, many discrete models of practical interest, such as metastable particle systems, are slowly mixing. There is also a large class of systems arising as discretizations of PDE models of heterogeneous media. For such models, the smallest relevant scale is still much large than larger than the average distance between molecules. Thus relaxation times may be comparable to observation time, especially if the observation time is chosen arbitrarily (this is often the case for PDE problems, while most ODE-specific tools are designed for studying long-time behavior).

Despite significant progress in multiscale methods, development of effective closures for non-linear heterogeneous problems with arbitrary relaxation times remains an open issue. Many current effective models for non-linear phenomena rely heavily on phenomenological closures. For example, in models of flow and reactive transport in porous media, phenomenology is used to describe the dependence of soil and rock permeability and capillary pressure on saturation of fluid phases and the relationship between effective reaction and dispersion coefficients on flow, diffusion, and reaction rates [25]. Due to heavy reliance on phenomenology, error estimates in these models are difficult to obtain.

This paper is devoted to developing a dimension reduction method for large size ODE models that define fluid flow at the microscale. At the heart of the method is a computational closure based on an iterative deconvolution for estimation of fine-scale variables from the corresponding averages. The main advantage of the proposed closure is that it is not based on the assumption of fast mixing, short relaxation times, and approximate ergodicity. As a result, the method can be applied to investigating transient phenomena, as well as simulating hydrodynamic

behavior of non-ergodic systems including flows of multiphase fluids.

The starting point of the proposed dimension reduction method is the non-local balance equations obtained by spatial averaging of a system of ODEs for Newtonian particle dynamics [26,1].

While in many dimension reduction methods only a small subset of (slow varying) unknowns of the original (large) ODE system is simulated, here we consider an evolution of a suitable set of functionals-space hydrodynamic averages. This is a natural choice because these quantities are experimentally measurable and can be related to continuum mechanics.

The proposed dimension reduction method consists of the following basic steps:

(1) Choose a mesoscale by selecting space and time resolution parameters. The spatial resolution parameter generates a mesoscopic mesh. The number of mesh nodes, though large, is much smaller than the number of particles. This fact leads to computational savings. The problem geometry and relevant length scales are shown in Figure 1.
(2) Write down evolution balance equations (these are typically PDEs) for primary variables. In the typical situation of negligible thermal effects, the primary variables are mesoscale density and mesoscale velocity. Some of the evolution PDEs contain fluxes. The main example of such flux is a stress tensor in the momentum balance equation. The fluxes have explicit formulas expressing them as functions of particle positions and velocities. These formulas are exact but not useful for computation, because using them requires solving the original, large size ODE system.
(3) Use a numerical closure — numerically estimate the non-local fluxes. This is the key part of the proposed dimension reduction method. The computational closure is based on a regularized deconvolution. The deconvolution produces stable approximations of the interpolants of particle positions and velocities from the given values of the corresponding averages. At each time step, particles are uniformly or randomly distributed such that the particle densities correspond to the mesoscale density and the particle velocities are found from the regularized deconvolution of the mesoscale velocities. Then, the particle positions and velocities are used to calculate the non-local fluxes, and new mesoscale variables are found from the time integration of the evolution PDEs. The important fact here is that the operation count is determined by the mesoscale resolution. Thus it is much smaller that the number of operations needed to solve the original ODEs.

We use the model reduction method to solve a system of Smoothed Particle Hydrodynamic (SPH) ODEs describing single phase and two-phase layered Poiseuille flows driven by uniform and periodic (in space) body forces. We show that for the single phase Poiseuille flow driven by the uniform force, the accurate coarse so-

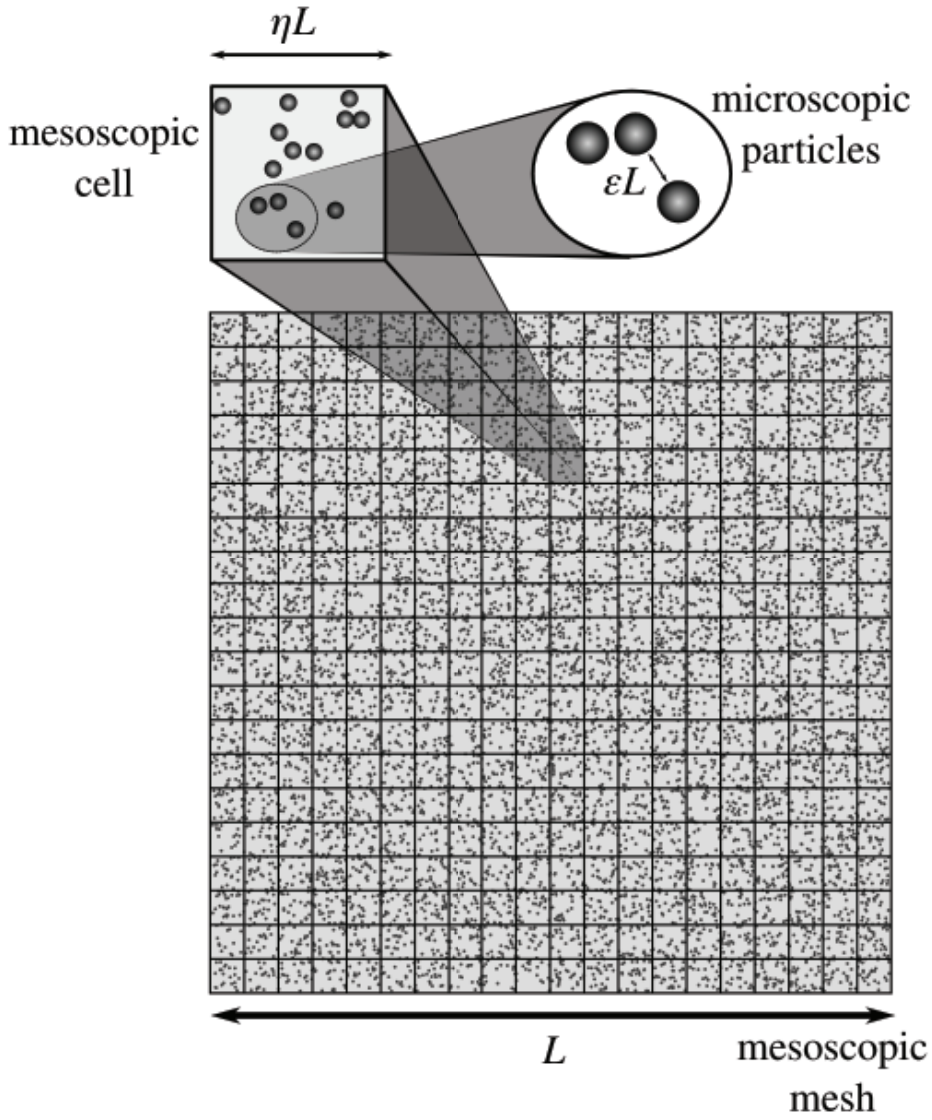

Fig. 1. Domain Ω with particles, mesoscopic mesh, and three length scales.

lution can be obtained with the zero-order deconvolution. For the single phase flow driven by the periodic body force and for the layered flow driven by the uniform force, the higher-order (first- and second-order) deconvolutions are necessary to obtain the accurate solution. The second-order deconvolution

The paper is organized as follows. In Section 2, we formulate the microscale model and recall the derivation of mesoscale balance equations. Section 3 is devoted to integral approximations of discrete sums that appear in the definitions of averages. In Section 4, we outline the basics of iterative deconvolution method for closure, and discuss the simplest zero-, first- and second-order approximations of microscale velocities. Section 5 contains an application of the zero-order closure to coarse graining of SPH discretization of the gravity-driven Poiseuille

flow equations. In Section 6, the first-order closure is applied to coarsening of the Poiseuille flow driven by a spatially periodic body force. In the section 7, the meso-scale balance equations with the second-order closure are used to coarse-grain SPH multiphase flow equations. Conclusions are given in Section 8. The paper also contains several appendices, providing details of explicit calculations and deriving partial error estimates.

2 Mesoscale Evolution Equations

2.1 Microscale problem

To define the averages, we first formulate the microscale ODE problem. The positions $\boldsymbol{q}_i(t)$ and velocities $\boldsymbol{v}_i(t)$ of particles P_i satisfy a system of Newton equations:

$$\dot{\boldsymbol{q}}_i = \boldsymbol{v}_i, \tag{2.1}$$

$$m_i \dot{\boldsymbol{v}}_i = \boldsymbol{f}_i + \boldsymbol{f}_i^{(ext)}, \tag{2.2}$$

with the initial conditions

$$\boldsymbol{q}_i(0) = \boldsymbol{q}_i^0, \qquad \boldsymbol{v}_i(0) = \boldsymbol{v}_i^0. \tag{2.3}$$

Here, m_i is the mass of particle i, and $\boldsymbol{f}_i^{(ext)}$ denotes external forces, such as gravity. The interparticle forces $\boldsymbol{f}_i = \sum_j \boldsymbol{f}_{ij}$, where $\boldsymbol{f}_{ij}$ are pair interaction forces that depend on the relative positions and velocities of the respective particles. The initial positions of particles are denoted by $\boldsymbol{q}_i^0$ and $\boldsymbol{v}_i^0$, respectively.

2.2 Mesoscale hydrodynamics of space-time averages

Our goal is to approximate dynamics of various mesoscopic space averages (density, velocity, stress etc). The averages are functions of the particle positions $\boldsymbol{q}_j$ and velocities $\boldsymbol{v}_j$.

Since averages are scale-dependent, we define three length scales:
- macroscopic length scale L is a typical size (diameter) of Ω;
- mesoscopic length scale $\eta' = \eta L$, where η is a parameter characterizing mesoscale spatial resolution;
- microscopic length scale $\varepsilon' = \varepsilon L$ with

$$\varepsilon = N^{-1/d}, \tag{2.4}$$

where N is the number of particles, and d is the dimension of the physical space, usually 1, 2, or 3.

To ensure scale separation, we require:

$$\varepsilon \ll \eta \ll 1. \tag{2.5}$$

To obtain the non-local evolution balance equations for the primary variables, we use a space averaging approach pioneered by Noll [27], and further developed in [26,1,28]. In this subsection we briefly recall the basic points of the method and introduce the relevant notation. The averages on the scale η are generated by a smooth function $\psi_\eta(\boldsymbol{x})$ that satisfies the normalization condition:

$$\int \psi_\eta(\boldsymbol{x})\, d\boldsymbol{x} = 1, \tag{2.6}$$

and decays sufficiently fast as $|\boldsymbol{x}| \to \infty$, where $\boldsymbol{x}$ is the Euclidean coordinate vector in a bounded domain Ω. Many choices of ψ are possible, but, here, we prefer to work with the Gaussian function:

$$\psi_\eta(\boldsymbol{x}) = \frac{1}{(\sqrt{\pi}\eta')^d} e^{-\frac{\boldsymbol{x}\cdot\boldsymbol{x}}{\eta'^2}}. \tag{2.7}$$

Then, it is possible to define the primary continuum variables on the scale ηL [1]. These variables are the mesoscale density:

$$\overline{\rho}^\eta(t,\boldsymbol{x}) = \sum_{j=1}^{N} m_j \psi_\eta(\boldsymbol{x} - \boldsymbol{q}_j(t)), \tag{2.8}$$

and the mesoscale velocity:

$$\overline{\rho}^\eta \overline{\boldsymbol{v}}^\eta(t,\boldsymbol{x}) = \sum_{j=1}^{N} m_j \boldsymbol{v}_j(t) \psi_\eta(\boldsymbol{x} - \boldsymbol{q}_j(t)). \tag{2.9}$$

In this notation, the overbar emphasizes that the mesoscale variables are obtained via space averaging. Differentiating $\overline{\rho}^\eta$ and $\overline{\rho}^\eta \overline{\boldsymbol{v}}^\eta$ in time and using the ODEs (2.1) and (2.2), one can obtain mesoscopic PDEs (MPDEs) describing conservation of mass [1]:

$$\partial_t \overline{\rho}^\eta + \mathrm{div}(\overline{\rho}^\eta \overline{\boldsymbol{v}}^\eta) = 0, \tag{2.10}$$

and conservation of the linear momentum [1]:

$$\partial_t(\overline{\rho}^\eta \overline{\boldsymbol{v}}^\eta) + \mathrm{div}(\overline{\rho}^\eta \overline{\boldsymbol{v}}^\eta \otimes \overline{\boldsymbol{v}}^\eta) = \mathrm{div}\boldsymbol{T}^\eta + \boldsymbol{F}^{(ext)}. \tag{2.11}$$

The stress $\boldsymbol{T}^\eta$ is expressed by [28]:

$$\boldsymbol{T}^\eta = \boldsymbol{T}^\eta_{(c)} + \boldsymbol{T}^\eta_{(int)},$$

where

$$\boldsymbol{T}^{\eta}_{(c)}(t,\boldsymbol{x}) = -\sum_{j=1}^{N} m_j(\overline{\boldsymbol{v}}^{\eta}(\boldsymbol{x}) - \boldsymbol{v}_j) \otimes (\overline{\boldsymbol{v}}^{\eta}(\boldsymbol{x}) - \boldsymbol{v}_j)\psi_{\eta}(\boldsymbol{x} - \boldsymbol{q}_j) \tag{2.12}$$

and

$$\boldsymbol{T}^{\eta}_{(int)}(t,\boldsymbol{x}) = \sum_{(j,k)} \boldsymbol{f}_{jk} \otimes (\boldsymbol{q}_k - \boldsymbol{q}_j) \int_0^1 \psi_{\eta}\Big(s(\boldsymbol{x} - \boldsymbol{q}_k) + (1-s)(\boldsymbol{x} - \boldsymbol{q}_j)\Big)\, ds. \tag{2.13}$$

The summation in j,k is over all pairs of particles (j,k) that interact with each other. The external force is given by:

$$\boldsymbol{F}^{(ext)}(t,\boldsymbol{x}) = \sum_{i=1}^{N} \boldsymbol{f}_i^{(ext)} \psi_{\eta}(\boldsymbol{x} - \boldsymbol{q}_i). \tag{2.14}$$

Discretizing MPDEs on the mesoscopic mesh yields a discrete system of equations, called the *meso-system*, written for mesh values of $\overline{\rho}^{\eta}_j$, $\overline{\boldsymbol{v}}^{\eta}_j$, and $\boldsymbol{T}^{\eta}_j$, $j = 1, J$. The number of grid points in the mesoscale mesh is $J = \eta'^{-d}$. The dimension of the meso-system is much smaller than the dimension of the original ODE problem, since $J \ll N$. However, at this stage, we still have no computational savings, since the meso-system is not closed. This means that the stress values $\boldsymbol{T}^{\eta}_j$ in MPDEs are functions of the microscopic positions and velocities. We emphasize that the system of MPDE equations (2.10)-(2.14) is exact (assuming that the microscale ODE model is exact), but solving it directly is prohibitively expensive because it requires solving the complete microscale system (2.1), (2.2). To achieve computational savings, one has to approximate mesoscopic fluxes, such as $\boldsymbol{T}^{\eta}_j$, using only the values of other mesoscopic quantities, such as the average density and velocity. We refer to the procedure of generating these approximations as a *computational closure method*.

3 Integral Approximations of Averages

The first step toward computational closure is to approximate sums by integrals in the formulas for stress and kinematic averages. For general particle dynamics ODE, this process is far from straightforward. The sums in Eqs. (2.8), (2.9), (2.12) and (2.13) do resemble Riemann sums. However, particle positions change in time, and particles are not periodically distributed in space. Because of this, a generic flow domain partition generated by positions $\boldsymbol{q}_j$ will be non-uniform — cells corresponding to different particles would have different volumes. In fact, existence of a uniform partition for each t seems to be a restriction that should be imposed on dynamics. Otherwise, the integral approximation should include the Jacobian of the microscopic flow map associated with the ODE dynamical

system. We shall not pursue these interesting questions here, leaving them to future publications.

Instead, we take advantage of the fact that discretizations of fluid flow PDEs can be generated so that this difficulty is not present. Fluid problems are typically written in spatial (Eulerian) description, and at each time the choice of discretization is up to us. As such, we can choose discretization nodes on a spatially uniform mesh. Of course, nodes that are uniformly spaced at the moment t_1, will be advected by the flow and not be (in general) uniformly spaced at $t_2 > t_1$. Thus, working with periodic meshes, at each time we actually change the physical identity of fluid particles, but this is not important as long as we wish to work only with *spatial* averages. In this paper we do not work with time averages, so we can make a standing assumption that the current particle positions are nodes of the periodic mesh, for example, a square mesh in two spatial dimensions with the mesh size L/ε, where $\varepsilon = N^{-1/2}$.

Next, we note that $\frac{m_j}{\rho_j} = |\Omega_j|$ (ρ_j is the microscale density and $|\Omega_j|$ is the volume associated with particle j) and interpret the sums in Eqs (2.8), (2.9), (2.12) and (2.13) as Riemann sums corresponding to the uniform partition of Ω with the partition cell volume $|\Omega|/N = |\Omega_j|$ ($j = 1, \ldots N$). This yields the integral approximation for meso-scale density:

$$\overline{\rho}^{\eta}(\boldsymbol{x}) = \int_{\Omega} \rho(\boldsymbol{x}')\psi_{\eta}(\boldsymbol{x}-\boldsymbol{x}')d\boldsymbol{x}', \tag{3.1}$$

and mesoscale momentum (dependence on t is suppressed for notational simplicity):

$$\overline{\rho}^{\eta}(\boldsymbol{x})\overline{\boldsymbol{v}}^{\eta}(\boldsymbol{x}) = \int_{\Omega} \rho(\boldsymbol{x}')\boldsymbol{V}^{\varepsilon}(\boldsymbol{x}')\psi_{\eta}(\boldsymbol{x}-\boldsymbol{x}')d\boldsymbol{x}', \tag{3.2}$$

where $\boldsymbol{V}^{\varepsilon}$ is a suitable microscopic velocity interpolant. For fluids with uniform density, we have:

$$\overline{\boldsymbol{v}}^{\eta}(\boldsymbol{x}) = \int_{\Omega} \boldsymbol{V}^{\varepsilon}(\boldsymbol{x}')\psi_{\eta}(\boldsymbol{x}-\boldsymbol{x}')d\boldsymbol{x}'. \tag{3.3}$$

The convectional component of the stress tensor is then:

$$\boldsymbol{T}^{\eta}_{(c)}(\boldsymbol{x}) = -\int_{\Omega} \rho(\boldsymbol{x}')(\overline{\boldsymbol{v}}^{\eta}(\boldsymbol{x}) - \boldsymbol{V}^{\varepsilon}(\boldsymbol{x}')) \otimes (\overline{\boldsymbol{v}}^{\eta}(\boldsymbol{x}) - \boldsymbol{V}^{\varepsilon}(\boldsymbol{x}'))\psi_{\eta}(\boldsymbol{x}-\boldsymbol{x}')d\boldsymbol{x}', \tag{3.4}$$

and the interaction component of the stress is:

$$\boldsymbol{T}^{\eta}_{(int)}(\boldsymbol{x}) = \frac{1}{2}\int_{\Omega}\int_{\Omega} \overline{\boldsymbol{f}}(\boldsymbol{V}^{\varepsilon}(\boldsymbol{x}'), \boldsymbol{V}^{\varepsilon}(\boldsymbol{x}''), \boldsymbol{x}', \boldsymbol{x}'') \otimes (\boldsymbol{x}''-\boldsymbol{x}') \int_0^1 \psi_{\eta}\left(s(\boldsymbol{x}-\boldsymbol{x}'') + (1-s)(\boldsymbol{x}-\boldsymbol{x}')\right) ds d\boldsymbol{x}' d\boldsymbol{x}''. \tag{3.5}$$

In Eq. (3.5),

$$\overline{\boldsymbol{f}}(\boldsymbol{V}^{\varepsilon}(\boldsymbol{x}'), \boldsymbol{V}^{\varepsilon}(\boldsymbol{x}''), \boldsymbol{x}', \boldsymbol{x}'') = n^{\star 2}\boldsymbol{f}(\boldsymbol{V}^{\varepsilon}(\boldsymbol{x}'), \boldsymbol{V}^{\varepsilon}(\boldsymbol{x}''), \boldsymbol{x}', \boldsymbol{x}''), \tag{3.6}$$

where the function $\boldsymbol{f}$ is defined by the equation describing interparticle forces via

$$\boldsymbol{f}_{ij} = \boldsymbol{f}(\boldsymbol{v}_i, \boldsymbol{v}_j, \boldsymbol{q}_i, \boldsymbol{q}_j),$$

and

$$n^\star = \frac{N}{|\Omega|}$$

is the particle concentration (number density).

4 Closure

4.1 Closure via regularized deconvolution. General approach

Our approach to constructing closures is based on a simple idea: the integral approximations of the averages are related to the corresponding microscopic quantities via convolutions with the Gaussian kernel ψ_η. These convolutions relate the primary mesoscopic variables, e.g., density and momentum, with microscopic quantities. Therefore, taking the values of primary variables provided by the mesoscale solver, we can recover the microscopic quantities by numerically inverting convolution operators. The results are inserted into equations for flux(es), such as stress in the momentum balance. This yields closed-form equations for primary variables. Simulating these new equations can be done efficiently on coarse grids in space-time.

Define an operator R_η by:

$$R_\eta[f](\boldsymbol{x}) = \int \psi_\eta(\boldsymbol{x}-\boldsymbol{y}) f(\boldsymbol{y}) d\boldsymbol{y}. \tag{4.1}$$

It is easy to check (using Fourier transform, for example) that R_η with a Gaussian kernel is injective. As such, there exists a single-valued inverse operator R_η^{-1}, that we call the *deconvolution operator*. Unfortunately, R_η is compact in $L^2(\Omega)$. Thus, R_η^{-1} is unbounded. This is the underlying reason for the popular belief that averaging destroys the high-frequency information contained in the microscopic quantities. In fact, this information is still there (inverse operator exists), but it is difficult to recover in a stable manner, because of unboundedness. This does not make the situation hopeless. Reconstructing f from the knowledge of $R_\eta[f]$) is a classical example of an unstable ill-posed problem (small perturbations of the right-hand side may produce large perturbations of the solution). The exact nature of the ill-posedness and methods of regularizing the problem are well investigated both analytically and numerically [29–33]. Accordingly, we interpret R_η^{-1} as a suitable regularized approximation of the exact operator. Many regularizing techniques are currently available: Tikhonov regularization, iterative methods,

reproducing kernel methods, maximum entropy method, dynamical system approach, and others. It is fortunate that this vast array of knowledge can be used for dimension reduction. On the conceptual level, our approach makes it clear that instability associated with ill-posedness is a fundamental difficulty in the process of closing continuum mechanics equations.

Recently, the classical Landweber iterative deconvolution method [34], [35] attracted attention as a means to achieve sub-scale resolution in large eddy simulation methods [36], [37], [38] of turbulence. A related method was proposed in [39]. In the simplest version of the Landweber method, approximations g_n to the solution of the operator equation

$$R_\eta[g] = \overline{g}^\eta \tag{4.2}$$

are generated by the formula

$$g_n = \sum_{k=0}^{n} (I - R_\eta)^n \overline{g}^\eta, \quad g_0 = \overline{g}^\eta. \tag{4.3}$$

The number n of iterations plays the role of regularization parameter. In (4.3), I denotes the identity operator. The first three low-order approximations are:

$$f^{(0)} = g \qquad n = 0, \tag{4.4}$$

$$f^{(1)} = g + (I - R_\eta)[g] \qquad n = 1, \tag{4.5}$$

$$f^{(2)} = g + (I - R_\eta)[g] + (I - R_\eta)^2[g] \quad n = 2. \tag{4.6}$$

Another classical method is Tikhonov regularization (see e.g. [30]), where the solution of (4.2) is approximated by g_α that solves

$$R_\eta[g_\alpha] + \alpha C[g_\alpha] = \overline{g}^\eta. \tag{4.7}$$

Here α is a regularization parameter, and C is a stabilizing operator. In practice, C can be an identity, or a a suitable differential operator such as Laplacian.

4.2 Computational implementation of deconvolution

The discretized version of the integral equation (4.2) is a linear system

$$A\boldsymbol{x} = \boldsymbol{b}. \tag{4.8}$$

The ill-posedness of the integral equation (4.2) is reflected in the spectral (for square A), or singular value (for rectangular A) decomposition. For instance, for a square A, the spectrum has no gaps, the smallest eigenvalues are close to zero,

while the largest eigenvalue is nearly 1. The condition number of A is typically large, and can be as large as the reciprocal of machine precision. The actual value of the condition number depends on the choice of ψ (smoother window functions such as Gaussian lead to larger condition numbers), and the size of the meshes used for discretization. A good reference for problems of this type is the book [40]. Many numerical methods are currently available. Besides Tikhonov and Landweber methods, one can use conjugate gradient method and truncated singular value decomposition (SVD). The conjugate gradient method is quite well known. The truncated SVD method consists of first computing the SVD of A, and then computing the regularized approximation of an exact solution by projecting onto the subspace spanned by singular vectors corresponding to the few largest singular values. Retaining singular vectors corresponding to smaller singular values produces a more accurate, but less stable, approximation. The choice of truncation is determined by the actual level of noise in the right hand side. It is customary to discard singular values of the size comparable to the magnitude of the expected right hand side error.

It is important to keep in mind that discretization introduces a minimal length scale for the features that can be reconstructed. The details of smaller size are lost. Because of ill-posedness, one can rarely achieve this maximal possible resolution. However, using sufficiently fine meshes in (4.8), one can always achieve the so-called sub-filter scale resolution, that is, recover the details that are smaller than the meso-scale ηL. When the averages are inspected visually, such details would be partially, or even completely, obscured. Deconvolution restores these details and thus improves the accuracy of a meso-scale simulation.

In this study we use (4.8) for approximating microscopic velocity. In this case, $\boldsymbol{x}$ is the microsopic velocity interpolant, rendered on a suitable uniform mesh, and $\boldsymbol{b}$ is the discretized average velocity, rendered on the coarse mesh. For discretizing microscopic velocity one could either use the same coarse mesh, or choose a finer mesh, even the finest mesh with N nodes.

In this work we use Landweber iteration because it is simple and useful for modeling. The drawback of this method is its rather slow convergence. Within the Landweber method, the first (zero-order) approximation is always the average itself. Subsequent iterations enhance higher frequency content. The low order discrete approximations corresponding to (4.4)-(4.6) are

$$\begin{aligned} \boldsymbol{x}_0 &= \boldsymbol{b}, \\ \boldsymbol{x}_1 &= \boldsymbol{b} + (I - A)\boldsymbol{b}, \\ \boldsymbol{x}_2 &= \boldsymbol{b} + (I - A)\boldsymbol{b} + (I - A)^2\boldsymbol{b}. \end{aligned} \tag{4.9}$$

For computational efficiency, the averages should be rendered on the coarse mesh. Then $\boldsymbol{x}_n$ in (4.9) are also rendered on the coarse mesh. To facilitate the computation of the stress, we interpolated these approximations to the fine mesh.

Linear interpolation was used on $\boldsymbol{b}$, and the terms containing powers of A were interpolated by replacing A with the coarse-fine quadrature of the convolution kernel. To give an example, the interpolated representation of $A\boldsymbol{b}$ is

$$(A\boldsymbol{b})_j = h\sum_{i=1}^{D}\psi_\eta(\boldsymbol{y}_j-\boldsymbol{x}_i)\boldsymbol{b}_i, \quad i=1,\ldots,D,\ j=1,\ldots,N,$$

where h is the fine mesh size, $\boldsymbol{y}_j$ are fine mesh points, and $\boldsymbol{x}_i$ are coarse mesh points.

Since $\boldsymbol{x}$ is a micro-scale quantity, a natural way to represent it is by using the fine mesh. Discretizing $\boldsymbol{x}$ on the coarse mesh introduces additional error, but greatly improves efficiency. The operation count of the deconvolution in this case depends only the number of coarse mesh points determined by the choice of η. Therefore, for very large N, the operation count will be independent of N and will remain fixed as long as η is fixed. This "coarse-coarse" discretization can be used for fast preliminary assessment and selective visualization of streaming data generated by a much slower ODE solver. Using a coarse mesh for the right hand side and a fine mesh for the solution is typically more accurate and at the same time more expensive. The computational cost scales roughly as $O(N)$. Using the fine mesh for both right hand side and the solution leads to even higher computational cost is of the order $O(N^2)$. This high cost does not necessarily corresponds to a better reconstruction, since discretization refinement generally increases the condition number of A.

4.3 Low-order closure equations for velocities

Let us consider the zero ($\boldsymbol{V}^{\varepsilon(0)}$) and first-order ($\boldsymbol{V}^{\varepsilon(1)}$) approximations of the microscopic velocity interpolant $\boldsymbol{V}^\varepsilon$. The microscopic velocity interpolant is related to the average velocity $\overline{\boldsymbol{v}}^\eta$ via:

$$R_\eta\left[\boldsymbol{V}^\varepsilon\right]=\overline{\boldsymbol{v}}^\eta. \tag{4.10}$$

The zero-order approximation corresponding to (4.4) is simply:

$$\boldsymbol{V}^{\varepsilon(0)}=\overline{\boldsymbol{v}}^\eta. \tag{4.11}$$

This means that the actual microscopic velocities are approximated by the mesoscopic average velocity at the same spatial points. Since mesoscopic average will be typically calculated on the mesoscale (coarse) grid, interpolation of the mesoscale velocity is needed for actual numerical implementation. The zero-order approximation is used in the paper to close mesoscopic algorithm for simulating Poiseuille flow driven by the uniform body force.

The first- and second order approximations are obtained from (4.5) as:

$$\boldsymbol{V}^{\varepsilon(1)} = \boldsymbol{V}^{\varepsilon(0)} + (I - R_\eta)[\overline{\boldsymbol{v}}^\eta] \tag{4.12}$$

and

$$\boldsymbol{V}^{\varepsilon(2)} = \boldsymbol{V}^{\varepsilon(0)} + (I - R_\eta)[\overline{\boldsymbol{v}}^\eta] + (I - R_\eta)^2[\overline{\boldsymbol{v}}^\eta]. \tag{4.13}$$

The first-order velocity fluctuations $\boldsymbol{U}^{\varepsilon(1)} = \boldsymbol{V}^{\varepsilon(1)} - \overline{\boldsymbol{v}}^\eta$ correspond to

$$\boldsymbol{U}^{\varepsilon(1)} = (I - R_\eta)[\overline{\boldsymbol{v}}^\eta]. \tag{4.14}$$

This means that microscopic velocity fluctuations are approximated by the convolution $I - R_\eta$ applied to the average velocity. Consider the kernel of this convolution operator. Its Fourier transform,

$$1 - e^{-\eta'^2\pi^2\boldsymbol{\xi}\cdot\boldsymbol{\xi}}, \tag{4.15}$$

is nearly zero for frequencies $|\xi|$ close to zero, and increases to 1 as $|\xi|$ goes to infinity. Therefore, $I - R^\eta$ acts as a filter damping low frequencies, emphasizing higher frequency content of the signal. For larger n, the approximations $\boldsymbol{U}^{\varepsilon(n)} = \sum_{k=1}^{n}(I - R_\eta)^k[\overline{\boldsymbol{v}}^\eta]$ will increasingly boost the high-frequency content. This suggests that larger velocity fluctuations should be handled with higher-order approximations. The first-order deconvolution is used here to close mesoscopic algorithm for simulating Poiseuille flow driven by the spatially periodic body force.

5 Coarse-Scale Solution of Smoothed Particle Hydrodynamics ODEs for Single-Phase Poiseuille Flow

5.1 SPH ODEs

To illustrate the proposed method, we present a coarse-grained solution of a system of SPH ODEs. In SPH, fluids are represented by material particles whose dynamics are governed by Eqs. (2.1)-(2.3). The interaction force in SPH can be obtained from a Lagrangian with added symmetric dissipation term [41]:

$$\boldsymbol{f}_{ij} = -\left(\frac{P_j}{n_j^2} + \frac{P_i}{n_i^2}\right)\nabla_i w_\varepsilon(\boldsymbol{q}_i - \boldsymbol{q}_j) + \frac{1}{2}\mu\frac{\boldsymbol{v}_i - \boldsymbol{v}_j}{n_i n_j|\boldsymbol{q}_i - \boldsymbol{q}_j|^2}(\boldsymbol{q}_i - \boldsymbol{q}_j)\cdot\nabla_i w_\varepsilon(\boldsymbol{q}_i - \boldsymbol{q}_j). \tag{5.1}$$

Here, $\boldsymbol{q}_i = [q_{x,i}, q_{y,i}]^T$ are particle positions, $\boldsymbol{v}_i(t)$ are velocities, μ is the fluid viscosity, and n_i are the number densities. The fluid pressure P_i is related to the number density through an equation of state, $P_i = P(n_i)$. Further, w_ε is the

smoothing function generating an SPH discretization. The smoothing function should have a compact support on the order of ε, satisfy the normalization condition:

$$\int w_\varepsilon(\boldsymbol{x})\,d\boldsymbol{x} = 1, \tag{5.2}$$

and approach the Dirac delta function in the limit of $|\boldsymbol{x}| \to 0$. Different forms of w_ε are discussed in [41].

Monaghan [41] showed that if the system of ODEs is obtained in this manner, then the particle system behaves as a Newtonian fluid. Under certain approximations, a system of ODEs also can be obtained from the Navier-Stokes equations [41–44].

Here, we consider a system of SPH ODEs that simulates a two-dimensional laminar flow of an incompressible fluid between two parallel plates located at $y = 3\eta'$ and $y = L_y - 3\eta'$. The SPH discretization is obtained by placing particles on a square lattice (with the lattice size equal to ε) in the domain $[0, L_x] \times [0, L_y]$. The flow is driven by an external force $\boldsymbol{f}_i^{ext}$ acting in x-direction. To simulate the no-slip boundary conditions at the plates, the velocities of the fluid particles outside the channel are set to zero [45]:

$$\boldsymbol{v}_i(t) = 0 \qquad q_{y,i} < 3\eta' \quad \text{or} \quad q_{y,i} > L_y - 3\eta'. \tag{5.3}$$

Initial velocities of all fluid particles are set to zero. A periodic flow (and the periodic pressure field) is assumed in the x direction.

5.2 Coarse-scale solution of the SPH ODEs using exact expression for the interaction stress

Under the conditions previously described, the y component of the mesoscale velocity is identically zero, and the mesoscale solution of the SPH equations is given by the MPDEs:

$$\frac{\partial \overline{v}_x^\eta(\boldsymbol{x})}{\partial x} = 0, \qquad \overline{v}_y^\eta \equiv 0, \tag{5.4}$$

$$\overline{\rho}^\eta \frac{\partial \overline{v}_x^\eta}{\partial t} = \frac{\partial (T^\eta_{(c),xx} + T^\eta_{(int),xx})}{\partial x} + \frac{\partial (T^\eta_{(c),xy} + T^\eta_{(int),xy})}{\partial y} + \overline{\rho}^\eta g, \tag{5.5}$$

subject to the boundary conditions,

$$\overline{v}_x^{\eta}(x,3\eta';t)=0 \qquad \text{and} \qquad \overline{v}_x^{\eta}(x,L_y-3\eta';t)=0. \tag{5.6}$$

The initial zero velocities of the SPH particles and Eq. (2.9) for the mesoscale velocity give rise to the initial condition for Eq. (5.5):

$$\overline{v}_y^{\eta}(x,y,0)=0. \tag{5.7}$$

It can be easily verified that for the considered Poiseuille flow $\partial_x T^{\eta}_{(c),xx}\equiv 0, \partial_y T^{\eta}_{(c),xy}\equiv 0$ and $\partial_x T^{\eta}_{(int),xx}\equiv 0$, and Eq (5.5) can be further simplified as:

$$\overline{\rho}^{\eta}\frac{\partial \overline{v}_x^{\eta}}{\partial t}=\frac{\partial T^{\eta}_{(int),xy}}{\partial y}+\overline{\rho}^{\eta}g. \tag{5.8}$$

Eq. (5.8) is solved with a finite differences method using a uniform mesh with the grid size η'. The number of grid points in x and y directions is given by $N_x^m=\frac{L_x}{\eta'}-1$ and $N_y^m=\frac{L_y}{\eta'}-1$, correspondingly. The coordinates of an ij-node are expressed by:

$$x_i=(i-0.5)\times\eta' \qquad i=1,...,N_x^m \tag{5.9}$$

and

$$y_j=(j-0.5)\times\eta', \qquad j=1,...,N_y^m. \tag{5.10}$$

A finite differences discretization of Eq. (5.8) subject to the boundary conditions (5.6) is:

$$\overline{v}^{\eta,t+\Delta t}_{x,ij}=\overline{v}^{\eta,t}_{x,ij}+\frac{\Delta t}{\Delta x\overline{\rho}^{\eta}}\left[T^t_{(i+1)j}-T^t_{ij}\right]+\Delta t g, \qquad i=2, \quad j=1,N_y^m, \tag{5.11}$$

$$\overline{v}^{\eta,t+\Delta t}_{x,ij}=\overline{v}^{\eta,t}_{x,ij}+\frac{\Delta t}{2\Delta x\overline{\rho}^{\eta}}\left[T^t_{(i+1)j}-T^t_{(i-1)j}\right]+\Delta t g, \qquad i=3,N_m-2, \quad j=1,N_y^m, \tag{5.12}$$

$$\overline{v}^{\eta,t+\Delta t}_{x,ij}=\overline{v}^{\eta,t}_{x,ij}+\frac{\Delta t}{\Delta x\overline{\rho}^{\eta}}\left[T^t_{ij}-T^t_{(i-1)j}\right]+\Delta t g, \qquad i=N_m-1, \quad j=1,N_y^m, \tag{5.13}$$

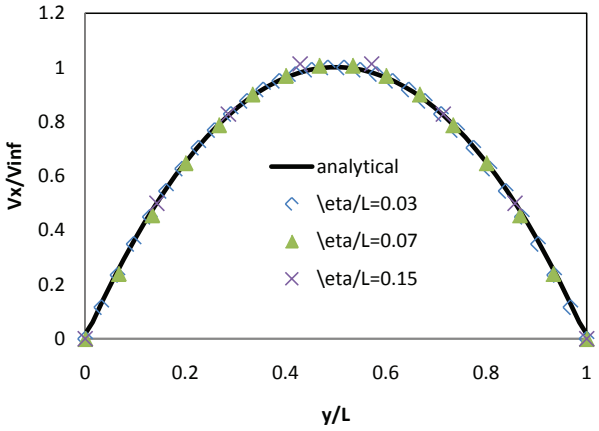

Fig. 2. Comparison of mesoscale steady state velocities with the analytical solution for different η

$$\overline{v}^{\eta,t}_{x,1j} = 0 \qquad \text{and} \qquad \overline{v}^{\eta,t}_{x,N_m j} = 0, \quad j = 1, N^m_y, \tag{5.14}$$

where T^t is used for $T^{\eta,t}_{(int),xy}$.

To estimate the interaction stress at time $t+\Delta t$, the particle velocities and particle positions should be found from the averages $\overline{\rho}^{\eta}_{ij}(t+\Delta t)$ and $\overline{\boldsymbol{v}}^{\eta}_{ij}(t+\Delta t)$. In SPH, particle positions are discretization points, and the natural choice is to place the particles uniformly in each lattice of the mesoscale mesh with the number of particles in the ij-lattice given by $\overline{\rho}^{\eta}_{ij}(t+\Delta t)\eta'^2/m^*$, where m^* is the mass of an SPH particle. In the considered case of the incompressible flow the position of SPH particles is kept intact. The velocities of the "fluid" SPH particles $\boldsymbol{v}_i(t+\Delta t) = \boldsymbol{V}^{\varepsilon(n)}_i(t+\Delta t)$ are found from the mesoscale velocities $\overline{\boldsymbol{v}}^{\eta}(\boldsymbol{x}, t+\Delta t)$ using the deconvolution Eq. (4.11) or Eq.(4.12) (or higher-order deconvolutions). The interaction stress $T^{\eta}_{(int),xy}$ is then calculated from Eq. (2.13).

For the incompressible flow, the particle density in Eq. (2.13) is constant and, for the considered SPH discretization, is equal to:

$$n^* = \frac{\overline{\rho}^{\eta}_{ij}}{m^*}.$$

The pressure $P^* = P(n^*)$ is the corresponding (constant) pressure, and the total number of the SPH particles is then equal to $N = L_x L_y n^*$. The integral in Eq. (2.13) for $T^{\eta}_{(int),xy}$ is evaluated analytically (see the Appendix A).

Figure 2 shows the comparison of the mesoscale fully developed (steady state)

velocity profiles with the analytical solution,

$$V_x(y) = -\frac{\rho g}{2\mu}\left[y^2 - (l_1 + l_2)\, y + l_1 l_2\right], \tag{5.15}$$

for different η'/L_y. Here $l_1 = 3\eta'$ and $l_2 = L_y - 3\eta'$. Eq. (5.15) is the solution of the steady state Navier-Stokes equation:

$$0 = -\frac{\partial P}{\partial x} + \mu\frac{\partial^2 V_x}{\partial y^2} + \rho g \qquad \mathbf{x} \in (-\infty, \infty) \times (l_1, l_2), \tag{5.16}$$

$$0 = -\frac{\partial P}{\partial y} \qquad \mathbf{x} \in (-\infty, \infty) \times (l_1, l_2), \tag{5.17}$$

$$V_y = 0 \qquad \mathbf{x} \in (-\infty, \infty) \times (l_1, l_2), \tag{5.18}$$

subject to the boundary conditions:

$$V_x = 0, \qquad y = l_1, l_2, \tag{5.19}$$

and

$$P = P_0, \qquad x = -\infty, \infty. \tag{5.20}$$

The figure shows an excellent agreement between the analytical and numerical results for small η'/L_y. The accuracy of the meso-scale method slightly decreases as η'/L_y increases. In the simulations shown in Figure 2, the zero-order deconvolution, Eq. (4.11), is used. It turns out to be quite accurate. We also demonstrate that in this example the velocity fluctuations are small (goes to zero as η'^2)(see Appendix B). This is done by computing the convective stress , which is essentially the covariance matrix of velocity fluctuations. The trace of this matrix is (essentially) the kinetic energy of velocity fluctuations. Smallness of kinetic energy is the underlying reason for a good accuracy obtained from the zero-order approximation.

5.3 Coarse-scale solution of the SPH ODEs using coarse approximation of the interaction stress

In the previous example, the interaction stress was found from Eq. (2.13). Unfortunately, this equation is expensive to evaluate, since it involves summing up about N terms for the short-range interactions $\boldsymbol{f}_{ij}$. This is the same number of operations (per time step) as in the SPH method, and the only (but significant) computational advantage over the direct SPH simulations in this example is achieved via an increase in the time step. The time steps in SPH and the dimensional reduction method are controlled by the Courant-Friedrichs-Lewy (CFL)condition and the constraint due to the viscous term:

$$\Delta t = \kappa_1 \frac{\Delta}{\boldsymbol{v}*} \tag{5.21}$$

and

$$\Delta t = \kappa_2 \frac{\rho \Delta^2}{\mu} \tag{5.22}$$

where $\boldsymbol{v}*$ is the maximum velocity, κ_1 and κ_2 are coefficients that are less then 1 (in the simulations these parameters are set to 0.25), $\Delta = \varepsilon'$ in the SPH model, and $\Delta = \eta'$ in the dimension reduction model. Since η' is much larger than ε, the time step in the dimension reduction model can be much larger than the time step in the SPH model. The computational advantage is more significant for the low Reynolds number flows (flows dominant by the viscous forces) when the time step increases as Δ^2 (according to the time constraint (5.22)) than for the high Reynolds number flow where the time step increases linearly with Δ (the time constraint (5.21)).

To further reduce the computational cost of the dimension reduction method, a coarse approximation of $\boldsymbol{T}^{\eta}_{(int)}$ is introduced. For the SPH interaction forces (5.1), the integral form of the interaction stress is:

$$\begin{aligned} \boldsymbol{T}^{\eta}_{(int)}(\boldsymbol{x}) = \frac{1}{2} \int_{\Omega_s} \int_{\Omega_s} \overline{\boldsymbol{f}}(\boldsymbol{x}', \boldsymbol{x}'', \boldsymbol{v}(\boldsymbol{x}'), \boldsymbol{v}(\boldsymbol{x}'')) \otimes (\boldsymbol{x}'' - \boldsymbol{x}') \\ \cdot \int_0^1 \psi_\eta \left(s(\boldsymbol{x} - \boldsymbol{x}'') + (1-s)(\boldsymbol{x} - \boldsymbol{x}') \right) ds d\boldsymbol{x}' d\boldsymbol{x}'', \end{aligned} \tag{5.23}$$

where

$$\begin{aligned} &\overline{\boldsymbol{f}}\,(\boldsymbol{x}', \boldsymbol{x}'', \boldsymbol{v}(\boldsymbol{x}'), \boldsymbol{v}(\boldsymbol{x}'')) \\ &= \left[-\rho(\boldsymbol{x}') \left(\frac{P(\boldsymbol{x}'')}{\rho(\boldsymbol{x}'')} + P(\boldsymbol{x}') \frac{\rho(\boldsymbol{x}'')}{\rho^2(\boldsymbol{x}')} \right) + \frac{1}{2} \mu \frac{\boldsymbol{v}(\boldsymbol{x}') - \boldsymbol{v}(\boldsymbol{x}'')}{|\boldsymbol{x}' - \boldsymbol{x}''|^2} (\boldsymbol{x}' - \boldsymbol{x}'') \right] \\ &\cdot \nabla_{\boldsymbol{x}'} w_\varepsilon(\boldsymbol{x}' - \boldsymbol{x}''). \end{aligned} \tag{5.24}$$

We start by introducing new variables:

$$\boldsymbol{R} = \frac{1}{2}(\boldsymbol{x}' + \boldsymbol{x}''), \qquad \boldsymbol{\rho} = \boldsymbol{x}' - \boldsymbol{x}'',$$

and re-writing the integral interaction stress (5.23) as:

$$\boldsymbol{T}^{\eta}_{(int)}(\boldsymbol{x}) = \frac{1}{2} \int_{\Omega} \int_{D_\varepsilon} \overline{\overline{\boldsymbol{f}}}(\boldsymbol{R}, \boldsymbol{\rho}) \otimes \boldsymbol{\rho} \int_0^1 \psi_\eta \left(s(\boldsymbol{x} - \boldsymbol{R} + \frac{1}{2}\boldsymbol{\rho}) + (1-s)(\boldsymbol{x} - \boldsymbol{R} - \frac{1}{2}\boldsymbol{\rho}) \right) ds\, d\boldsymbol{\rho}\, d\boldsymbol{R}, \tag{5.25}$$

where

$$\overline{\overline{\boldsymbol{f}}}(\boldsymbol{R},\boldsymbol{\rho}) = \overline{\boldsymbol{f}}\left(\boldsymbol{V}^{\varepsilon}(\boldsymbol{R}+\boldsymbol{\rho}/2), \boldsymbol{V}^{\varepsilon}(\boldsymbol{R}-\boldsymbol{\rho}/2), \boldsymbol{R}+\boldsymbol{\rho}/2, \boldsymbol{R}-\boldsymbol{\rho}/2\right). \tag{5.26}$$

An important observation about (5.25) is that the integration in $\boldsymbol{R}$ is still over the whole computational domain Ω, but integration in $\boldsymbol{\rho}$ is over a *much smaller domain* D_ε, which is the support of the microscale smoothing function w_ε. In case of non-compactly supported, but fast decreasing w_ε, such as Gaussian, we can take D_ε to be the ball of radius 3ε centered at zero. Such approximation can be easily justified using standard localization arguments. Another important observation is that the function ψ_η depending on $\boldsymbol{R}$ is a mesoscale quantity and, thus, varies slowly compared to $\boldsymbol{\rho}$-dependent functions. For low-compressible and incompressible fluids, the pressure and density are also slowly varied functions (or constants) in space. The velocity interpolant $\boldsymbol{V}^{\varepsilon}$ is not slowly varying, but it is approximated by a low-order (zero- or first-order) deconvolution, which does vary slowly. If one uses higher-order deconvolutions, defined in Eq. (4.3), the velocity approximations are still slowly varying, compared to $\boldsymbol{\rho}$-dependent functions.

To make use of this, we suggest using different grids for different integrals: the integral in $\boldsymbol{R}$ is discretized on a coarse mesh with a grid size on the order of η', while $\boldsymbol{\rho}$-integral is discretized on the fine mesh with a grid size on the order of ε'. Denote the nodes of the mesoscale mesh by $\boldsymbol{q}_\beta$, $\beta = 1,\dots,N_C$, $N_C \ll N$. The flow domain is subdivided into mesocells of area L_xL_y/N_C. The domain D_ε is subdivided into J cells of area $|D_\varepsilon|/J$, where J is the number of fine-scale mesh points surrounding a mesoscale mesh node and $|D_\varepsilon|$ is the area of D_ε. An efficient way of implementing this partition is to use the original fine-scale mesh for discretizing the $\boldsymbol{\rho}$-integral. In that case:

$$\frac{|D_\varepsilon|}{J} = \frac{L_xL_y}{N}.$$

Since $|D_\varepsilon| = \text{const}\cdot(L\varepsilon)^d = \text{const}\cdot(L_xL_y)/N$, J is independent of N. Approximating the integral (5.25) with its Riemann sum yields:

$$\begin{aligned}\boldsymbol{T}^{\eta}_{(int)}(t,\boldsymbol{x}) \approx \frac{1}{2}\sum_{\beta=1}^{N_C}\sum_{j=1}^{J}\frac{L_xL_y}{N_C}\frac{L_xL_y}{N}\overline{\boldsymbol{f}}(\boldsymbol{q}_\beta,\boldsymbol{\rho}_j) \\ \otimes\boldsymbol{\rho}_j\int_0^1\psi_\eta\left(s(\boldsymbol{x}-\boldsymbol{q}_\beta+\frac{1}{2}\boldsymbol{\rho}_j)+(1-s)(\boldsymbol{x}-\boldsymbol{q}_\beta-\frac{1}{2}\boldsymbol{\rho}_j)\right)ds\end{aligned} \tag{5.27}$$

The operation count of (5.27) depends on N_C and ζ, but not on N. Indeed, instead of summing up about N terms in (2.13), we now have N_CJ summations, and $N_C \ll N$, while J is independent of N. For fixed N_C, the asymptotics of the operation count in (5.27) is $O(1)$ as $N\to\infty$ compared to $O(N)$ in Eq. (2.13). As a consequence of comparative smallness of gradients of $\boldsymbol{R}$-dependent quantities in (5.27), the accuracy of this approximation is quite good. Figure 3 shows

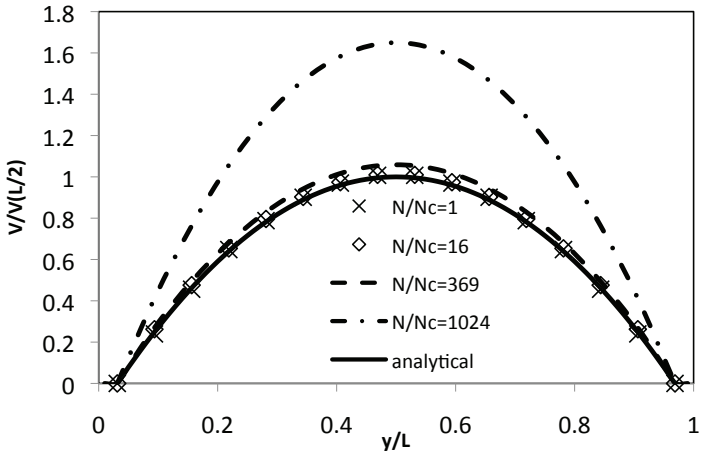

Fig. 3. Mesoscopic velocities obtained analytically (solid lines) and numerically (symbols and broken lines) using the coarsened approximation of the interaction stress. The ratio N/Nc is the reduction in the number of operations due to the coarse approximation of the interaction stress.

the comparison of the reduction method with the full and coarse estimations of the interaction stress and the analytical solution. The comparison shows a good agreement between the analytical solution and the model reduction model with N/N_C is as large as 369. The results obtained with $N/N_C = 16$ perfectly agree with the results of the model reduction model using the exact evaluation of the interaction stress ($N/N_C = 1$). In the computational examples presented above, the zero-order deconvolution was used to calculate SPH velocities. In the following section, we show the coarse approximation of the interaction stress is also accurate for the first-order deconvolution. In Appendix C, we present the analytical error estimates quantifying the accuracy of the coarse approximation of the interaction stress.

6 First-Order Deconvolution for Poiseuille Flow Driven by Periodic Body Force

Here, we consider a flow of incompressible fluid driven by the periodic body force:

$$\mu \frac{d^2 V_x(y)}{dy^2} + \rho g \left[1 + A \sin\left(\frac{y - l_1}{l_2 - l_1} n\pi \right) \right] = 0, \qquad l_1 < y < l_2 \tag{6.1}$$

subject to the same initial flow and boundary conditions as the Poiseuille flow with a uniform body force, described in the previous section. As before, the fluid was discretized with SPH particles, and the SPH ODEs were solved using the dimension reduction method. To describe oscillatory behavior of solution caused

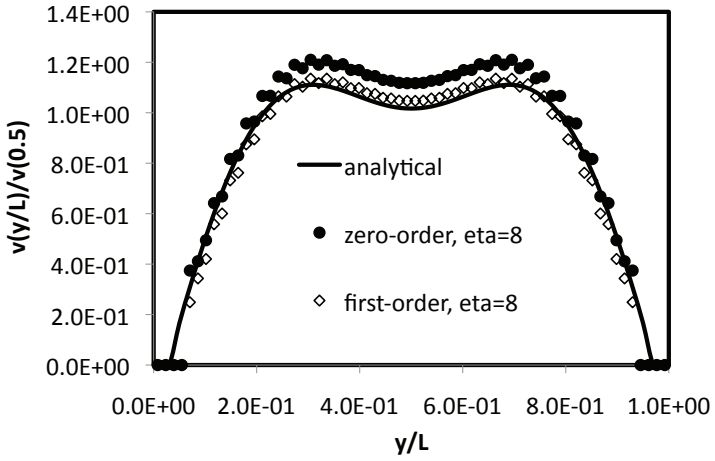

Fig. 4. Mesoscopic velocities obtained analytically (solid lines) and numerically (symbols and broken lines) using the zero- and first-order deconvolution of particles velocities. The coarsened approximation with $N/Nc = 32$ and $\eta/L = 0.07$ are used in the simulations.

by the periodic body force, here we use the first-order deconvolution. Figure 4 shows the comparison of the solutions obtained with the zero- and first-order deconvolutions and the analytical solution (see Appendix D). The comparison shows that the first-order solution is more accurate than the zero-order solution. These results also show that the coarse approximation of the interaction stress with $N/N_C = 64$ does not introduce a significant error into the first-order solution.

7 Coarse-Scale Solution of Smoothed Particle Hydrodynamics ODEs for Two-Phase Flow

Finally, we apply the dimension reduction method to multi-scale multi-phase flow. We consider two-fluid system in a two-dimensional channel where thin layers of less viscous fluid are randomly distributed in a more viscous fluid. All layers are oriented parallel to the walls of the channel of the width L. The mesoscale length in the simulations is set to $\eta' = L/16$, or $\eta = 1/16$. The microscale length is $\varepsilon' = L/192$ ($\varepsilon = 1/192$). To make the problem multiscale, we consider three different flows with the layers with thickness much smaller than the width of the channel. In Cases 1 and 2, the layers width is $3\eta'/4$ and in Case 3 the width of the layers is $9\eta'/4$. The distribution of layers in the three cases is shown in Fig 5.

In Case 1, the distance between some of the layers is on the order of the width of the layers. In Cases 2 and 3, the distance between all layers is much larger than the width of the layers.

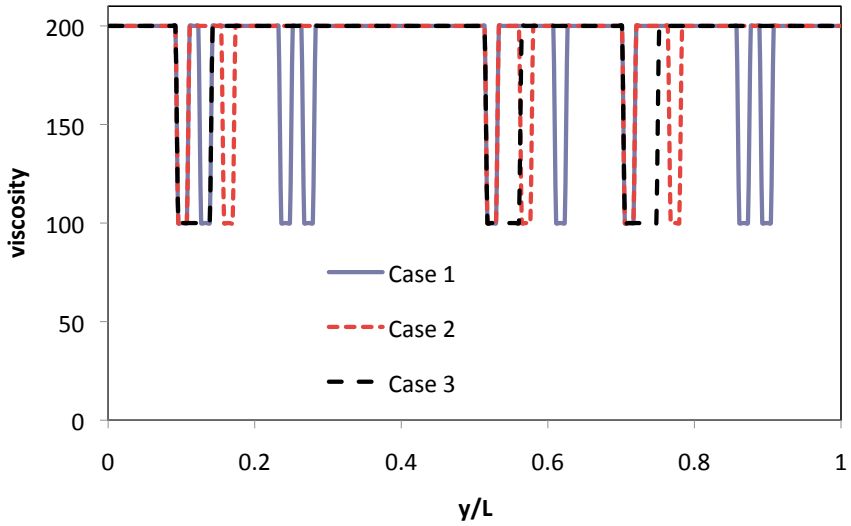

Fig. 5. Distribution of viscosity in the computational domain for the three test cases.

In the SPH multiphase flow model [44], different fluids are modeled by separate sets of particles. The dynamics of each set of particles is governed by Eqs (2.1), (2.2) and (5.1) that are closed with the van der Waals equation of state [44]:

$$P_i = \frac{n_i k_b T}{1 - c_1 n_i} - k_{ij} c_2 n_i^2. \tag{7.1}$$

In the equation of state, k_B is the Boltzman constant, T is the temperature (assumed here to be constant) and c_1 and c_2 are the van der Waals constants (assumed here to be the same for all fluids). The parameter k_{ij} is set to 1 when interacting particles i and j are of the same fluid and to $k^* < 1$ for interaction between particles of different fluids. The surface tension between two fluids increases with decreasing k^*. We assume that the two fluids have the same density (masses of all particles are set the same). The viscosity ratio is set to two. The distributions of layers in the three considered cases are shown in Fig 5 where the viscous fluid has density of 200 (in the model units) and less viscous fluid has viscosity of 100 (in the model units). The initial velocity of the particles is set to zero and flow is initiated by applying a uniform constant body force in the direction parallel to the walls of the channel. We set the surface tension large enough (k^* is small enough) so that, in the absence of initial perturbations in the layers geometry, no Kelvin-Helmholtz instability developed and flow remained laminar and stable for the entire time in the SPH simulations. The direct solutions of SPH equations for the three cases are depicted in Figs 6 - 8.

It should be noticed that in all three cases the widths of the layers are smaller than the size (diameter) of the averaging window that is equal to $6\eta'$, and in the coarse scale calculations the layers of the less viscous fluid represent a sub-scale feature, the feature that cannot be explicitly resolved on the coarse scale. Fur-

thermore, the micro-scale flow is a mixture of two non-Newtonian fluids. Therefore, the effective rheology on the meso-scale is unknown at present, though it is likely to be non-Newtonian as well. Because of this, the closed form of the coarse scale momentum conservation equations is not available. Consequently, direct coarse scale simulations are not possible.

In the coarse solution, obtained with the dimension reduction method, the flow is assumed incompressible and the average velocities are found from Eqs (5.11)-(5.14). The coarse approximation, Eq (5.27), of T_{int} is used in the coarse-scale solution. The second order deconvolution is used in the simulations, because the lower order deconvolutions were found to produce significantly less accurate results. The coarse solutions of SPH equations, obtained with the dimension reduction method, are shown with diamond symbols. For times close to the initial moment, the coarse solutions agree with the direct solutions of the SPH equations for all cases. For later times, at which the solutions are almost reached the steady state, the agreement is the best (Fig 6, the maximum error is within 2%) for Case 3 and the worse (Fig 8, the maximum error is within 10 %). In the second case the maximum error is within 6%. The error is calculated as a relative difference between maximum velocities obtained from coarse and direct solutions of SPH equations at the time when the flow is assumed to reach the steady state (the time after which solution changes by less than 0.001% after 1000 time steps). The dimension reduction method is the most accurate when the smallest continuum feature, which needs to be resolved, has a characteristic length greater or equal to η'. In Case 3, the width of the layers is $2.25\eta'$ and the dimension reduction method has the smallest error of 2%. In Case 2, the layer width is slightly smaller than η' but the distance between the layers is much larger than η' and this results in the error of 6%. In Case 1, when both the width of the layers and the distance between some of the layers is smaller than η' the error is the highest (10%). Our results show that in all considered cases the error decreases with decreasing η' but this leads to the increasing computational cost.

8 Conclusions

We developed a dimension reduction method for large size ODE systems arising as discretization of fluid flow models. The proposed method is applicable to other Newtonian particle dynamics ODEs, both conservative and dissipative, with nearly constant particle concentration, such as periodic lattice problems modeling small amplitude vibrations. The method relies on a computational closure of evolution balance equations, obtained by space averaging of the ODEs. For isothermal flows, the balance equations are the continuity equation and the momentum conservation equation. The latter contains a non-local flux term - a stress tensor that is an explicit function of particle positions and velocities. The closure method is based on a simple idea: the integral approximations of the

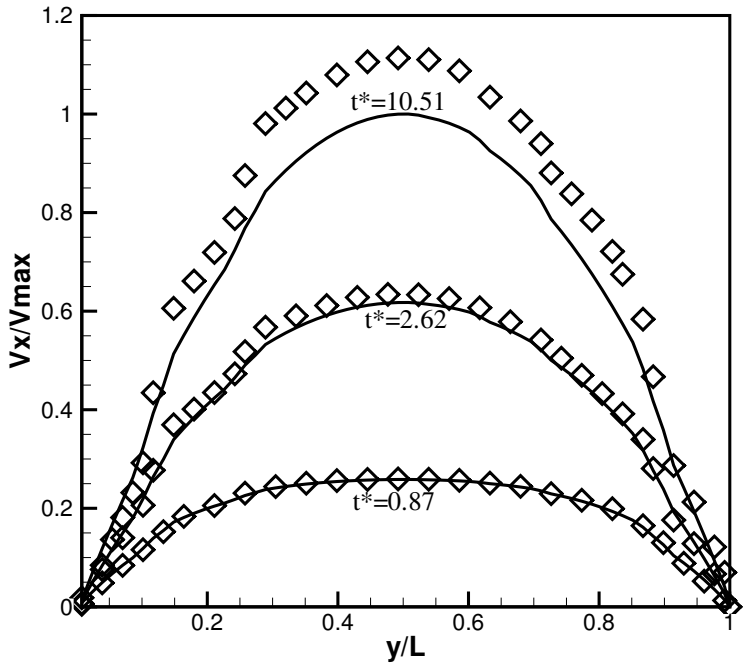

Fig. 6. Case 1: Comparison of coarse and direct solutions of the SPH equations at different dimensionless times $t^* = t v_{max}/L$. v_{max} is the maximum velocity at the largest time, at which flow reached the steady-state profile.

averages are related to the corresponding microscopic quantities via a convolution operator. These convolutions relate the primary mesoscopic variables, e.g., density and momentum, with microscopic quantities. Therefore, taking the values of primary variables provided by the mesoscale solver, we can approximately recover the microscopic quantities by iteratively inverting the convolution operator. Computational savings are produced by increasing the time step (the time step for integration of balance equations is much larger than the time step for integration of the underlying ODEs), and reducing the number of operations at each time step.

To illustrate the computational advantages of the proposed reduction method, we used it to solve a system of Smoothed Particle Hydrodynamic ODEs describing single- and two-phase layered Poiseuille flows driven by uniform and periodic (in space) body forces. For the single-phase Poiseuille flow driven by the uniform force, the accurate coarse solution was obtained with the zero-order deconvolution. For the single-phase flow driven by the periodic body force, the first-order deconvolution was necessary to obtain the accurate solution. In the two-phase flow problem we studied the layered flow of two fluids with the width of the layers of the less viscous fluid being much smaller than the size of the channel. We found that an accurate coarse scale solution was possible to achieve with the meso-scale parameter on the order of the size of the layers using the

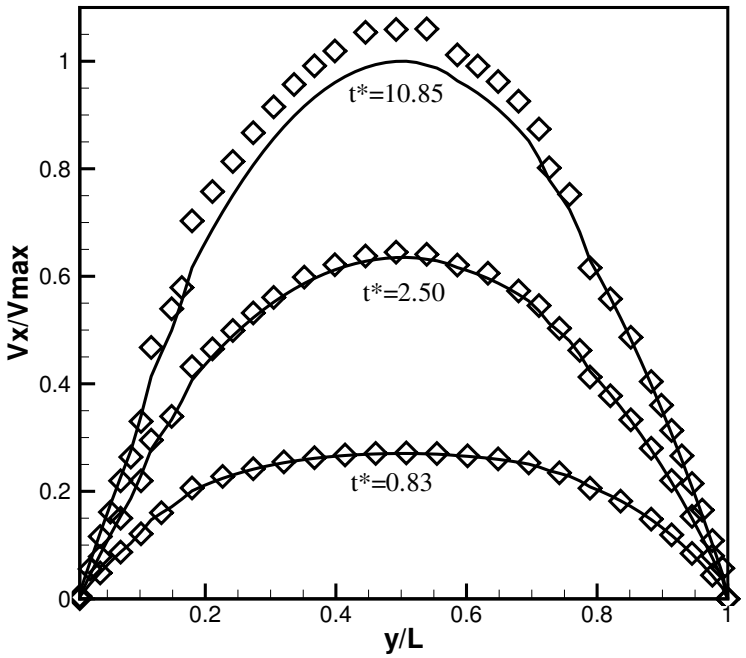

Fig. 7. Case 2: Comparison of coarse and direct solutions of the SPH equations at different dimensionless times $t^* = t v_{max}/L$. v_{max} is the maximum velocity at the largest time, at which flow reached the steady-state profile.

second-order deconvolution. It should be emphasized that the coarse scale solution was obtained without any assumptions on the effective rheological properties of the two-fluid system at the meso-scale.

The deconvolution-based closure is a general idea that can be used, in principle, for more general Newtonian particle models exhibiting mixing and strong inhomogeneity of particle distribution. Another promising area of application is development of fast numerical simulations of mesoscale behavior of mixtures of several fluids, flows with fluid-solid interactions and other models of highly heterogeneous continuum systems. Our preliminary results do not allow us to comment on the possible accuracy of the method for these type of problems, but they do show that the method can be accurate for multiscale problems with non-uniform distribution of particle properties on the meso-scale.

A Integral in the Interaction Component of the Meso Stress

The integral of the weighting function in (3.5) is:

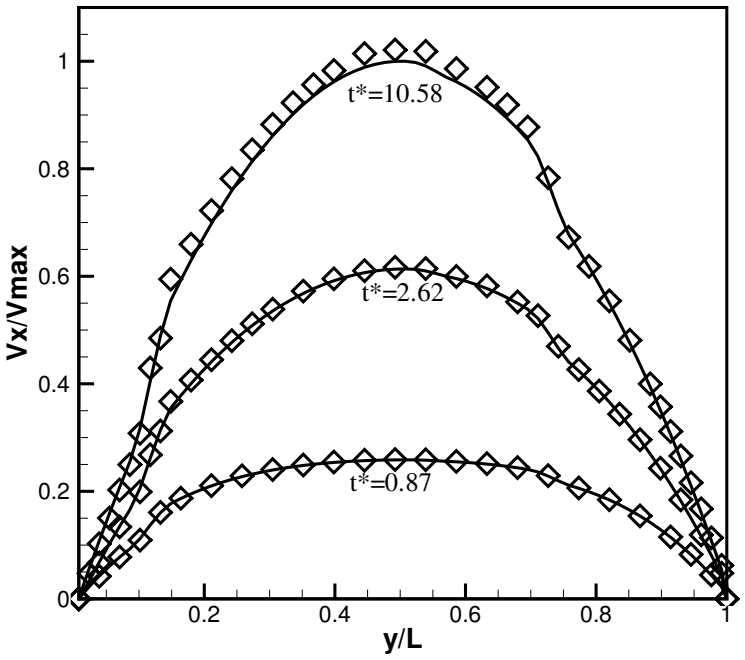

Fig. 8. Case 3: Comparison of coarse and direct solutions of the SPH equations at different dimensionless times $t^* = tv_{max}/L$. v_{max} is the maximum velocity at the largest time, at which flow reached the steady-state profile.

$$\frac{1}{\pi\eta^2}\int_0^1 e^{-\frac{\left(s(\boldsymbol{x}-\boldsymbol{x}'')+(1-s)(\boldsymbol{x}-\boldsymbol{x}')\right)^2}{\eta^2}}\,ds = \frac{1}{2\sqrt{\pi}\eta|\boldsymbol{x}'-\boldsymbol{x}''|}e^{ab^2-c}\left[\mathrm{erf}\left(b\sqrt{a}+\frac{1}{2\sqrt{a}}\right)-\mathrm{erf}\left(b\sqrt{a}\right)\right] \tag{A.1}$$

where

$$\frac{1}{4a} = \frac{(x'-x'')^2+(y'-y'')^2}{\eta^2} = \frac{|\boldsymbol{x}'-\boldsymbol{x}''|^2}{\eta^2} \qquad \text{or} \qquad a = \frac{\eta^2}{4|\boldsymbol{x}'-\boldsymbol{x}''|^2} \tag{A.2}$$

$$b = \frac{2[(x'-x'')(x-x')+(y'-y'')(y-y')]}{\eta^2} = \frac{2(\boldsymbol{x}'-\boldsymbol{x}'')\cdot(\boldsymbol{x}-\boldsymbol{x}')}{\eta^2} = 2b', \tag{A.3}$$

and

$$c = \frac{(x-x')^2+(y-y')^2}{\eta^2} = \frac{|\boldsymbol{x}-\boldsymbol{x}'|^2}{\eta^2}. \tag{A.4}$$

B Convectional Stress

For the Poiseuille flow driven by the uniform body force, the only non-zero component of the convectional stress (3.4) is the T_{xx} component:

$$-T^{\eta}_{(c),xx}(\boldsymbol{x})/\rho = \int_{\Omega} (\overline{v}^{\eta}_{x}(\boldsymbol{x}) - V^{\varepsilon}_{x}(\boldsymbol{x}'))^2 \psi_{\eta}(\boldsymbol{x}-\boldsymbol{x}')\, d\boldsymbol{x}' \tag{B.1}$$
$$= \int_{\Omega} V^{\varepsilon}_{x}(\boldsymbol{x}')^2 \psi_{\eta}(\boldsymbol{x}-\boldsymbol{x}')\, d\boldsymbol{x}' - \overline{v}^{\eta}_{x}(\boldsymbol{x})^2.$$

The (only non-zero) x component of the steady state mesoscale velocity can be found by performing analytical integration of Eq (3.3) with $\boldsymbol{V}^{\varepsilon}$ given by the analytical steady-state solution for the Poiseuille flow. The steady state mesoscale velocity is given by:

$$\bar{v}^{\eta}_{x}(y) = -\frac{\rho g}{2\mu}\left[\frac{\eta^2}{2} + y^2 - (l_1+l_2)\,y + l_1 l_2\right]. \tag{B.2}$$

The last integral in Eq. (B.1) can be evaluated analytically, resulting in the following expression for the steady state convectional stress:

$$-T^{c}_{xx}(y)/\rho = \frac{\rho^2 g^2}{4\mu^2}\left[\frac{1}{4}\eta^4 + \frac{(l_1+l_2-2y)^2}{2}\eta^2\right] - \frac{\rho g}{2\mu}\overline{v_x}(y)\eta^2 + V_x(y)^2 - \overline{v_x}(y)^2.$$

C Error Estimate of the Coarse Discretization of Zero-Order Interaction Stress

Here, we estimate the error incurred by replacing the fine-scale discretization (2.13) of the interaction stress with a coarse-scale discretization (5.27). We only deal with a one-dimensional case. Generalizing to higher dimensions is straightforward. The inter-particle force formulas are taken from the SPH equations (5.1).

First, introduce some notation. Pick a number $c \in (0,1)$ and let q_β be coarse mesh points $\beta = 1,2,\ldots,B$. The computational domain in $\Omega = (0,L)$, and the coarse mesh step size is:

$$\Delta_c = c\eta L.$$

The number of these points is:

$$B = \frac{1}{c\eta}.$$

The corresponding coarse-scale cells C_β are intervals of length Δ_c. Each cell contains several fine-scale cells $C_{\beta,i}$, $i \in I_\beta$, where I_β denotes the set of indices of the

included cells. The number of fine-scale cells within a coarse-scale cell is:

$$|I_\beta| = \frac{c\eta}{\varepsilon}.$$

In one-dimension and a uniform pressure field, Eq. (5.1) reduces to:

$$f_{ij} = \frac{1}{2}\mu\frac{L^2}{N^2}\frac{v_i - v_j}{|q_i - q_j|^2}(q_i - q_j)\,w'_\varepsilon(q_i - q_j).$$

In the zero-order approximation, v_i, v_j are replaced by $\overline{v}^\eta(q_i), \overline{v}^\eta(q_j)$, respectively. The fine-scale discretization of the interaction stress in the zero-order approximation is (compare with (2.13)):

$$T_{(f)} = \frac{1}{2}\mu\frac{L^2}{N^2}\sum_{i=1}^{N}\sum_{j\in J}(\overline{v}^\eta(q_i) - \overline{v}^\eta(q_j))\,w'_\varepsilon(q_i - q_j)\int_0^1 \psi_\eta(s(x-q_j)+(1-s)(x-q_i))\,ds. \tag{C.1}$$

Changing variables from q_i, q_j to $R_i + \frac{1}{2}\rho_j, R_i - \frac{1}{2}\rho_j$ as in Section 5 and writing $R_i = q_\beta + \Delta R_i$, for each $i \in I_\beta$, from (C.1) we obtain:

$$T_{(f)} = \frac{1}{2}\mu\frac{L^2}{N^2}\int_0^1 \sum_{\beta=1}^{B}\sum_{j\in J} w'_\varepsilon(\rho_j)\sum_{i\in I_\beta} A_{i,j,\beta}(x,s)\,ds, \tag{C.2}$$

where

$$A_{i,j,\beta}(x,s) = \left(\overline{v}^\eta(q_\beta + \Delta R_i + \frac{1}{2}\rho_j) - \overline{v}^\eta(q_\beta + \Delta R_i - \frac{1}{2}\rho_j)\right)\psi_\eta(x - q_\beta - \Delta R_i + \frac{1-2s}{2}\rho_j).$$

The coarse discretization of the interaction stress is:

$$T_{(c)} = \frac{1}{2}\mu\frac{L^2}{N^2}|I_\beta|\int_0^1 \sum_{\beta=1}^{B}\sum_{j\in J} w'_\varepsilon(\rho_j)\left(\overline{v}^\eta(q_\beta + \frac{1}{2}\rho_j) - \overline{v}^\eta(q_\beta - \frac{1}{2}\rho_j)\right)\psi_\eta(x - q_\beta + \frac{1-2s}{2}\rho_j). \tag{C.3}$$

Next, we write,

$$T_{(f)} = T_{(c)} + S_1 + S_2 + S_3,$$

where

$$S_1 = \frac{1}{2}\mu\frac{L}{B}\frac{L}{N}\frac{B}{N}\int_0^1 \sum_{\beta=1}^{B}\sum_{j\in J}\sum_{i\in I_\beta}|\rho_j|\,w'_\varepsilon(\rho_j)\left(\Delta\overline{v}^\eta(R_i) - \Delta\overline{v}^\eta(0)\right)\psi_\eta\left(x - q_\beta + (1-2s)\frac{\rho_j}{2}\right)ds, \tag{C.4}$$

$$S_2 = \frac{1}{2}\mu\frac{L}{B}\frac{L}{N}\frac{B}{N}\int_0^1 \sum_{\beta=1}^{B}\sum_{j\in J}\sum_{i\in I_\beta}|\rho_j|\,w'_\varepsilon(\rho_j)\Delta\overline{v}^\eta(0)\Delta\psi_\eta(\Delta R_i)\,ds, \tag{C.5}$$

$$S_3 = \frac{1}{2}\mu\frac{L}{B}\frac{L}{N}\frac{B}{N}\int_0^1 \sum_{\beta=1}^{B}\sum_{j\in J}\sum_{i\in I_\beta}|\rho_j|\,w'_\varepsilon(\rho_j)\left(\Delta\overline{v}^\eta(\Delta R_I) - \Delta\overline{v}^\eta(0)\right)\Delta\psi_\eta(\Delta R_i)\,ds. \tag{C.6}$$

In Eqs. (C.4)-(C.6),

$$\Delta\overline{v}^{\eta}(h) = \frac{\overline{v}^{\eta}(q_\beta + \frac{1}{2}\rho_j + h) - \overline{v}^{\eta}(q_\beta - \frac{1}{2}\rho_j + h)}{|\rho_j|}$$

$$\Delta\psi_\eta(h) = \psi_\eta\left(x - q_\beta - h + (1-2s)\frac{\rho_j}{2}\right) - \psi_\eta\left(x - q_\beta + (1-2s)\frac{\rho_j}{2}\right).$$

To estimate the error, we need to estimate $S_i, i = 1,2,3$. To do this, we assume two bounds on the average velocity:

$$|\Delta\overline{v}^{\eta}(0)| \le M_1, \tag{C.7}$$

with M_1 independent of c, ε, η; and

$$|\Delta\overline{v}^{\eta}(h) - \Delta\overline{v}^{\eta}(0)| \le \omega(h) \tag{C.8}$$

where $\omega(h)$ is a positive, continuous, decreasing function with $\lim_{h\to 0}\omega(h) = 0$, independent of c, η, ε.

Estimating S_1. By (C.8):

$$\frac{B}{N}\left|\sum_{i\in I_\beta}\Delta\overline{v}^{\eta}(R_i) - \Delta\overline{v}^{\eta}(0)\right| \le \frac{B}{N}\omega(\frac{1}{2}c\eta L)|I_\beta| = \omega(\frac{1}{2}c\eta L). \tag{C.9}$$

Thus,

$$|S_1| \le \frac{1}{2}\mu\omega(\frac{1}{2}c\eta L)\int_0^1 \sum_{\beta=1}^{B}\frac{L}{B}\sum_{j\in J}\frac{L}{N}|\rho_j|\,w'_\varepsilon(\rho_j)\psi_\eta\left(x - q_\beta + (\frac{1}{2} - s)\rho_j\right). \tag{C.10}$$

Recall that ψ_η is an even, positive, compactly supported function that has maximum at zero and decreases away from this maximum (a cut-off Gaussian is an example of such function). Using these properties of ψ_η, we deduce:

$$\sum_{\beta=1}^{B}\frac{L}{B}\psi_\eta\left(x - q_\beta + (\frac{1}{2} - s)\rho_j\right) \le \sum_{\beta=1}^{B}\frac{L}{B}\psi_\eta\left(\frac{L}{2} - q_\beta\right) \le \int_0^L \psi_\eta\left(\frac{L}{2} - y\right)dy \le 1. \tag{C.11}$$

Finally, setting $\rho_j = \varepsilon\hat{\rho}_j$, we arrive at:

$$\sum_{j\in J}\frac{L}{N}|\rho_j||\omega'_\varepsilon(\rho_j)| \le \varepsilon L\varepsilon\varepsilon^{-2}\sum_{j\in J}|\hat{\rho}_j||\omega'(\hat{\rho}_j)| \le M_2, \tag{C.12}$$

where M_2 is independent of c, η, ε. Combining (C.10), (C.11), and (C.12) to obtain:

$$|S_1| \le \frac{1}{2}\mu M_2\omega(\frac{1}{2}c\eta L). \tag{C.13}$$

Estimating S_2. First, set $\Delta R_i = c\eta\Delta\hat{R}_i$ and note that:

$$\left|\frac{L}{N}\sum_{i\in I_\beta}\Delta\psi_\eta(\Delta R_i)\right| \le \varepsilon L\frac{1}{\eta}\sum_{i\in I_\beta}\left|\psi\left(\frac{x-q_\beta+(\frac{1}{2}-s)\rho_j}{\eta}-c\Delta\hat{R}_i\right)-\psi\left(\frac{x-q_\beta+(\frac{1}{2}-s)\rho_j}{\eta}\right)\right|$$
$$\le cL\frac{\varepsilon}{\eta}\sup|\psi'|\sum_{i\in I_\beta}|\Delta\hat{R}_i| \tag{C.14}$$
$$\le \frac{\varepsilon^2}{\eta^2}L^2\sup|\psi'||I_\beta|$$
$$= c\frac{\varepsilon}{\eta}L^2\sup|\psi'|.$$

Using this inequality and (C.7), we obtain:

$$|S_2| \le \frac{1}{2}\mu c\frac{\varepsilon}{\eta}L^2\sup|\psi'|M_1\sum_{\beta=1}^{B}\sum_{j\in J}\frac{L}{N}|\rho_j||w'_\varepsilon(\rho_j)|$$

Finally using (C.12), we find:

$$|S_2| \le \frac{1}{2}\mu L^2M_1M_2\sup|\psi'|c\frac{\varepsilon}{\eta}B = \frac{1}{2}\mu M_1M_2L^2\sup|\psi'|\frac{\varepsilon}{\eta^2}. \tag{C.15}$$

where M_1, M_2 are constants from (C.7) and (C.12), respectively.

Estimating S_3. Use of (C.8) yields:

$$|S_3| \le \frac{1}{2}\mu\omega(\frac{1}{2}c\eta L)\int_0^1\sum_{\beta=1}^{B}\sum_{j\in J}\frac{L}{N}|\rho_j||\omega'_\varepsilon(\rho_j)|\sum_{i\in I_\beta}\frac{L}{N}|\Delta\psi_\eta(\Delta R_i)|ds.$$

This sum is exactly as the one that appeared in estimating S_2. Therefore, we can use (C.14) and (C.12) to find:

$$|S_3| \le \frac{1}{2}\mu\omega(\frac{1}{2}c\eta L)BM_2cL^2\sup|\psi'|\frac{\varepsilon}{\eta} = \frac{1}{2}\mu L^2\sup|\psi'|M_2\omega(\frac{1}{2}c\eta L)\frac{\varepsilon}{\eta^2}. \tag{C.16}$$

Now, combining estimates (C.13), (C.15) and (C.16) yields the overall error bound:

$$|T_{(f)}-T_{(c)}| \le \frac{1}{2}\mu M_2\left(\omega(\frac{1}{2}c\eta L)+M_1L^2\sup|\psi'|\frac{c\varepsilon}{\eta^2}+L^2\sup|\psi'|\frac{c\varepsilon}{\eta^2}\omega(\frac{1}{2}c\eta L)\right). \tag{C.17}$$

This inequality means that the error can be made small by choosing c and ε/η sufficiently small. We are interested in the situation when $\eta \in (0,1)$ is fixed and $\varepsilon \to 0$. Then, the second and third terms in the right-hand side go to zero, and the first term can be made arbitrarily small by choosing c small enough, or, equivalently, decreasing the coarse mesh size. This increases computational cost, and our estimate can be used to achieve a desired balance between cost and accuracy.

D Poiseuille Flow Driven by Periodic Body Force

Consider the steady state flow driven by the periodic body force:

$$\mu \frac{d^2 V_x(y)}{dy^2} + \rho g \left[1 + A \sin\left(\frac{y - l_1}{l_2 - l_1} n\pi \right) \right] = 0, \qquad l_1 < y < l_2 \tag{D.1}$$

subject to the boundary conditions:

$$V_x(y) = 0, \qquad y = l_1, \qquad \text{and} \qquad y = l_2. \tag{D.2}$$

Integrating the flow equations twice and applying the boundary conditions yields the analytical expression for the velocity:

$$V_x(y) = \frac{\rho g}{2\mu} \left[(l_1 + l_2) y - l_1 l_2 \right] - \frac{\rho g}{\mu} \left[\frac{y^2}{2} - A \frac{(l_2 - l_1)^2}{n^2 \pi^2} \sin\left(\frac{y - l_1}{l_2 - l_1} n\pi \right) \right], \qquad l_1 < y < l_2. \tag{D.3}$$

Acknowledgment

This work was supported by the Office of Advanced Scientific Computing Research founded by the U.S. Department of Energy. Pacific Northwest National Laboratory is operated for the U.S. Department of Energy by Battelle under Contract DE-AC05-76RL01830.

References

[1] A. Murdoch, D. Bedeaux, Continuum equations of balance via weighted averages of microscopic quantities, Proc. Royal Soc. London A 445 (1994) 157–179.

[2] S. Whitaker, The method of volume averaging, Kluver Academic Press, Dordrecht, the Nethelands, 1999.

[3] V. V. Zhikov, S. M. Kozlov, O. A. Oleinik, Homogenization of differential operators and integral functionals, Springer-Verlag, 1994.

[4] A. Braides, A. Derfanceschi, Homogenization of multiple integrals, Clarendon Press, 1998.

[5] A. Pankov, *G*-convergence and homogenization of nonlinear partial differential operators, Kluwer Academic Publishers, 1997.

[6] A. M. Tartakovsky, G. Redden, P. Lichtner, T. Scheibe, P. Meakin, Mixing-induced precipitation: experimental study and multi-scale numerical analysis, Water Resources Research 44 (2008) W06S04.

[7] A. M. Tartakovsky, D. M. Tartakovsky, P. Meakin, Stochastic langevin model for flow and transport in porous media, Physical Review Letters 101 (2008) 044502, DOI: 10.1103/PhysRevLett.101.044502.

[8] A. M. Tartakovsky, G. D. Tartakovsky, T. D. Scheibe, Effects of incomplete mixing on multicomponent reactive transport, Advances in Water Resources 32 (2009) 1674–1679.

[9] I. Battiato, D. Tartakovsky, A. Tartakovsky, T. Scheibe, On breakdown of macroscopic models of mixing-controlled heterogeneous reactions in porous media, Advances in Water Resources 32 (2009) 1664–1673.

[10] C. W. Gear, I. G. Kevrekidis, Projective methods for stiff differential equations: problems with gaps in their eigenvalue spectrum, SIAM J. Sci. Comput 24 (2003) 1091.

[11] M. E. Kavousanakis, R. Erban, A. Boudouvis, C. Gear, I. Kevrekidis, Projective and coarse projective integration for problems with continuous symmetries, J. Comput. Phys. 225 (1) (2007) 382–407.

[12] C. W. Gear, I. Kevrekidis, Constraint-defined manifolds: a legacy code approach to low-dimensional computation, J. Sci. Comput. 25 (1-2) (2005) 17–28.

[13] C. W. Gear, T. Kaper, I. Kevrekidis, A. Zagaris, Projecting to a slow manifold: singularly perturbed systems and legacy codes, SIAM J. Appl. Dyn. Syst. 4 (3) (2005) 711–732.

[14] A. Chorin, O. Hald, R. Kupferman, Prediction from partial data, renormalization, and averaging, J. Sci. Comput. 28 (2-3) (2006) 245–261.

[15] A. Chorin, O. Hald, R. Kupferman, Optimal prediction with memory, Phys. D 166 (3-4) (2002) 239–257.

[16] H. Mori, Transport collective motion and brownian motion, Progress of Theoretical Physics 33 (3) (1965) 423–&.

[17] R. Zwanzig, Collision of a gas atom with a cold surface, J. Chem. Phys. 32 (1960) 1173–1177.

[18] H. Maris, L. Kadanoff, Teaching the renormalization group, American J. Phys. 46 (1978) 652–657.

[19] P. R. Kramer, A. J. Majda, Stochastic mode reduction for the immersed boundary method, SIAM J. Appl. Math 64 (2) (2003) 369–400.

[20] M. A. Katsoulakis, P. Plechac, L. Rey-Bellet, Numerical and statistical methods for the coarse-graining of many-particle stochastic systems, J. Sci. Comput. 37 (43) (2008) ??71.

[21] M. Katsoulakis, A. Majda, D. Vlachos, Coarse-grained stochastic processes for microscopic lattice systems, Proc. Natl. Acad. Sci. 100 (3) (2003) 782.

[22] M. Katsoulakis, A. Majda, D. Vlachos, Coarse-grained stochastic processes and monte carlo simulations in lattice systems, J. Comput. Phys. 112 (2003) 250.

[23] M. Katsoulakis, P. Plechac, A. Sopasakis, Error analysis of coarse-graining for stochastic lattice dynamics, SIAM J. Numer. Anal. 44 (6) (2006) 2270.

[24] G. Pavliotis, A. M. Stuart, Multiscale methods. Averaging and homogenization, Springer, 2008.

[25] J. Bear, Dynamics of fluids in porous media, Dover Publications, New York, 1988.

[26] R. Hardy, Formulas for determining local properties in molecular-dynamics simulations: Shock waves, Journal of Chemical Physics 76 (1982) 622Ð628.

[27] W. Noll, Die herleitung der grundgleichungen der thermomechnik der kontinua aus der statistischen mechanic, Journal of Rational Mechanics and Analysis 4 (5) (1955) 627–646.

[28] A. I. Murdoch, A critique of atomistic definitions of the stress tensor, J Elasticity 88 (2007) 113–140.

[29] C. W. Groetsch, The Theory of Tikhonov Regularization for Fredholm Equation of the First Kind, Pitman, Boston, 1984.

[30] A. Kirsch, An Introduction to the Mathematical Theory of Inverse Problems, Springer, New York, 1996.

[31] Morozov, Methods for Solving Incorrectly Posed Problems, Springer, New York, 1984.

[32] A. Neubauer, An a posteriori parameter choice for tikhonov regularization in the presence of modeling error, Appl. Numer. Math. 4 (1988) 507–519.

[33] A. N. Tikhonov, V. Arsenin, Solutions of Ill-Posed Problems, Wiley, New York, 1987.

[34] V. Fridman, A method of successive approximations for fredholm integral equations of the first kind, Uspekhi Mat. Nauk (Russian) 11 (1956) 233–234.

[35] L. Landweber, An iteration formula for fredholm integral equations of the first kind, Am. J. Math. 73 (1951) 615–624.

[36] N. A. Adams, S. Stolz, Deconvolution methods fo subgrid-scale approximation in large-eddy simulaiton, in B. Geurts, ed., Modern simulation strategies for turbulent flows (2001) 21–41.

[37] N. A. Adams, S. Stolz, A subgrid-scale deconvolution approach for shock capturing, J. Comp. Phys 178(2) (2002) 391–426.

[38] L. C. Berselli, T. Iliescu, W. J. Layton, Mathematics of Large Eddy Simulation of Turbulent Flows, Springer, 2006.

[39] J. A. Domaradzki, N. A. Adams, Direct modeling of subgrid scales of turbulence in large eddy simulations, J. Turbulence 3 (24) (2002) 1–19.

[40] P. C. Hansen, Rank-Deficient and Discrete Ill-Posed Problems: Numerical Aspects of Linear Inversion, SIAM, 1987.

[41] J. Monaghan, Smoothed particle hydrodynamics, Rep. Progr. Phys. 68 (2005) 1703 – 1759.

[42] J. Morris, P. Fox, Y. Zhu, Modeling low reynolds number incompressible flows using sph, J. Comput. Phys. 136 (1997) 214.

[43] A. M. Tartakovsky, P. Meakin, Pore-scale modeling of immiscible and miscible flows using smoothed particle hydrodynamics, Advances in Water Resources 29 (2006) 1464–1478.

[44] A. M. Tartakovsky, K. F. Ferris, P. Meakin, Multi-scale lagrangian particle model for multiphase flows, Computer Physics Communications 180 (2009) 1874–1881.

[45] A. M. Tartakovsky, P. Meakin, Simulation of free-surface flow and injection of fluids into fracture apertures using smoothed particle hydrodynamics, Vadose Zone Journal 4 (3) (2005) 848–855.